ACS Photonics

pubs.acs.org/journal/apchd5

Article

Free-Space Diffused Light Collimation and Concentration

Published as part of the ACS Photonics virtual special issue "Photonics for Energy".

Lisanne M. Einhaus,[†] Geert C. Heres,[†] Jelle Westerhof, Shweta Pal, Akshay Kumar, Jian-Yao Zheng, and Rebecca Saive*

Cite This: *ACS Photonics* 2023, 10, 508–517

Read Online

ACCESS | Metrics & More | Article Recommendations

ABSTRACT: Collimating and concentrating broad-band diffused light can increase the yield, decrease the cost, and open new opportunities for solar-generated electricity. Adherence to the second law of thermodynamics requires that collimation, and therefore the reduction of étendue or entropy, of diffused sunlight, i.e., light scattered by clouds or the atmosphere, can only occur if the photons lose energy during the process. This principle has been demonstrated in luminescent solar concentrators; solar photons are energetically down-shifted by a luminophore and the emitted photons are trapped within a transparent matrix and guided toward an edge lining solar cell. However, this process suffers from low efficiency as the photons are trapped within the waveguide for a long time, encountering many instances of accumulating loss mechanisms. Here, we theoretically describe and experimentally demonstrate the first free-space diffused light collimation system which overcomes these efficiency losses. The high photon energy solar spectrum is allowed to enter the system from all angles, whereas the re-emitted luminescent photons can only escape under a desired emission cone. We achieved this through doping a polymethylmetacrylate waveguide with Lumogen Red dye, which we cover on one side with a Lambertian reflector for photon recycling and induced randomization and on the top face with a complex multilayer dielectric nanophotonic coating stack. We experimentally found an angular concentration of 118% within the designed escape cone, where isotropic emission corresponds to 100%, thereby verifying the reduction of étendue in free space experimentally. Such free-space collimation systems will enable efficient redirection of sunlight toward solar panels, thereby increasing yield, decreasing heating through the emission of low energy photons, and expanding the range of available surfaces from which sunlight can be harvested.

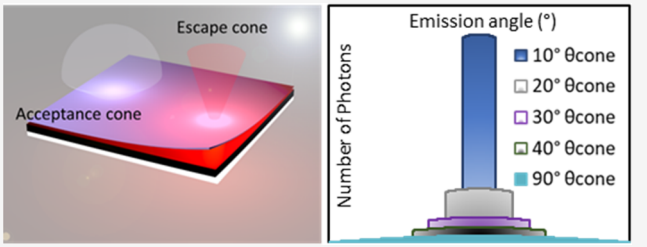

KEYWORDS: *diffused light, light concentration, photonic metamaterials, solar energy, spectro-angular emission, notch filters*

INTRODUCTION

Whether attempting to ignite a fire using a lens or operating a concentrator solar power plant, one will find it impossible during a fully overcast day, as both processes require a collimated light beam. The desire to turn diffuse light into a collimated beam may appear to violate the second law of thermodynamics[1,2] at first glance. Diffused light has a significantly larger étendue than a collimated beam. This means the collimation of light requires the reduction of entropy and therefore, the use of energy.[1,2] This energy can be obtained from down-shifting the photon frequency. Many light-driven applications only efficiently convert a fraction of the photon's energy, so the resulting system efficiency is not disadvantaged by down-shifting photons if a material with a suitable band gap is used. A prominent example is a solar cell: only the fraction of the photon's energy corresponding to the semiconductor band gap can be converted into electrical energy, whereas the excess energy of the photon is lost as heat.[3] Illuminating solar cells with red-shifted, narrow band light yields two benefits: it reduces heating and allows more efficient light management strategies.[4,5] Both lead to an increased yield and decreased cost for solar-generated electricity.

This principle has been demonstrated in solar cells with down-shifting coatings or luminescent solar concentrators (LSCs).[6−8] So far, none of these strategies have surpassed the yield of a conventional silicon solar cell.[9] Down-converters directly integrated on top of solar cells usually lead to other undesired (light) losses that have so far been hindering efficiency improvements. Luminescent solar concentrators have so far been limited to 7.1%[10,11] as significant

Received: October 20, 2022
Published: January 31, 2023

concentration inherently also increases the losses.[12] A further disadvantage of LSCs is that special solar cells are required to be integrated with the waveguides, often requiring millimeter-size cells and high-precision assembly. Nevertheless, concentrating light is beneficial for the yield and efficiency of a solar energy harvesting system. Concentrator optics that are spatially separated from the solar cell have led to record power conversion efficiencies of up to 47.1%.[13] However, these geometric optical concentrators need collimated light directly incident from the sun and require tracking of the solar path.[1] On the other hand, low light concentration can be achieved by placing solar panels into highly reflective surroundings and using this reflected "albedo" in addition to the directly incident light.[14] This approach also provides benefits during cloudy conditions.[15] Collimating and concentrating diffused light in free space combines all these advantages and opens up new possibilities for solar energy conversion.

We propose, analytically describe, and experimentally verify a nanophotonic free-space light collimation system, transforming the solar spectrum's diffuse, high-energy photons into a down-shifted, collimated beam. Unlike previously presented down-conversion and concentrating strategies for solar cells, our system introduces a spatial separation between the concentrator and the solar cell. This induces the advantages of geometric concentrators without necessitating direct, collimated sunlight as a prerequisite. Such a system omits the need for tracking, making applications on mechanically fixed structures, such as buildings, possible.

Nanophotonic Diffused Light-Collimation System. A schematic of the operation principle is shown in Figure 1:

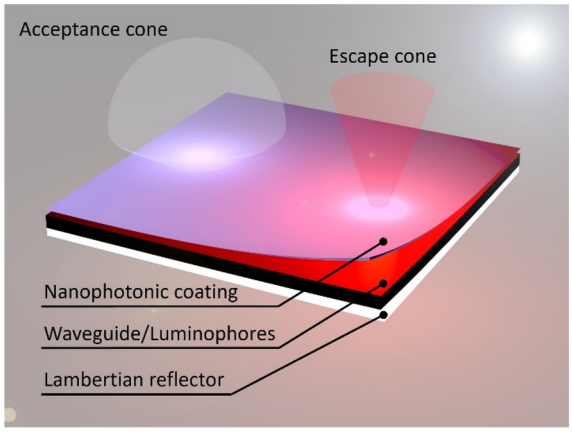

Figure 1. Schematic of free-space diffused light collimation achieved by photon down-shifting, randomization, recycling, and spectro-angular selective emission through a nanophotonic coating.

incoming photons are accepted by the nanophotonic coating within the acceptance cone spanning the full upper hemisphere. Luminophores embedded in a transparent polymer matrix down-shift, i.e., Stokes-shift, the energy of the photons. A Lambertian reflector at the bottom of the polymer ensures trapping, i.e., photon recycling[16] and randomization of the photons. The down-shifted photons falling within the escape cone are allowed to exit the structure, whereas photons outside of the escape cone will be reflected back into the structure. The Lambertian reflector recycles and randomizes these photons such that they obtain a chance to exit through the escape cone after a second pass through the structure. Note that for reciprocity reasons, within the narrow emission wavelength window of the luminophore and outside of the acceptance cone, also incident photons will be reflected off the nanophotonic coating. Contrary to conventional luminescent solar concentrators,[12] these photons should not be regarded as loss, but in our free-space configuration, they might still contribute to the irradiance of the solar panel in the same way a conventional specular mirror would if placed in the vicinity of the panel.[14] We developed an analytical model[17] to calculate the emission profile of our diffused light-collimation system depending on realistic material parameters that we will present in the following.

Analytical Description of Free-Space Concentration. A detailed balance model allows to calculate the steady-state of the system, i.e., the concentration of photons within the waveguide and within the escape cone for constant photon influx through the acceptance cone. Let us first consider the ideal case, in which all incoming blue photons can enter the waveguide, are converted into red photons and can only leave the waveguide through the designed escape cone. In this case, the whole system runs at 100% quantum efficiency as no photons are lost through the usual loss mechanisms, i.e., reflection, nonunity luminophore quantum yield, reabsorption, transmission at the bottom, and parasitic transmission outside of the escape cone or due to scattering or absorption in the substrate.

Let $\Delta\Omega_{in}$ be the angular spread of the incoming light which at first we assume to be perfectly randomized and isotropic, and $\Delta\Omega_{out}$ is the solid angle of the escape cone in free space (after refraction). This is shown schematically in Figure 1. If the radiance of the incoming light is L_{in} in units of photons per second per steradian, then the total incoming photon flux is $L_{in}\Delta\Omega_{in}$ [photons per second]. Similarly, the emitted radiance is L_{out} [photons per second per steradian], and the total emitted photon flux is $L_{out}\Delta\Omega_{out}$. In the ideal case, all photons that enter the structure are converted and emitted in the escape cone. This means that the incoming and emitted intensities must be equal. This results in the following equality:

$$L_{in}\Delta\Omega_{in} = L_{out}\Delta\Omega_{out}$$

Next, we will introduce a metric to quantify the collimation of the light, in other words, its angular concentration C, which is the ratio of L_{out} to L_{in} within the desired escape cone. For brevity, we will refer to this metric simply as concentration factor for the remainder of this paper. In a perfect Lambertian reflector, C is unity, as all photons would be reflected with acceptance and escape cone being identical. Diffused light collimation is achieved whenever C becomes larger than 1. The ideal concentration factor C_{id} in a system without losses can be calculated as follows:

$$C_{id} = \frac{L_{out}}{L_{in}} = \frac{\Delta\Omega_{in}}{\Delta\Omega_{out}}$$

This shows that in a system without losses the concentration factor is given by the ratio between the acceptance and escape cones as the photons are simply redistributed over a smaller escape cone. The ideal concentration is plotted in Figure 2a as a function of the escape cone half angle for a three-dimensional escape cone of 10°, 30°, 60°, and 90° (=Lambertian reflector), respectively. It shows that without losses, significant concentration can be achieved. Note that integrating all the shown curves in three dimensions assuming spherical symmetry yields the same total number of photons, as the photons are merely

https://doi.org/10.1021/acsphotonics.2c01652
ACS Photonics 2023, 10, 508−517

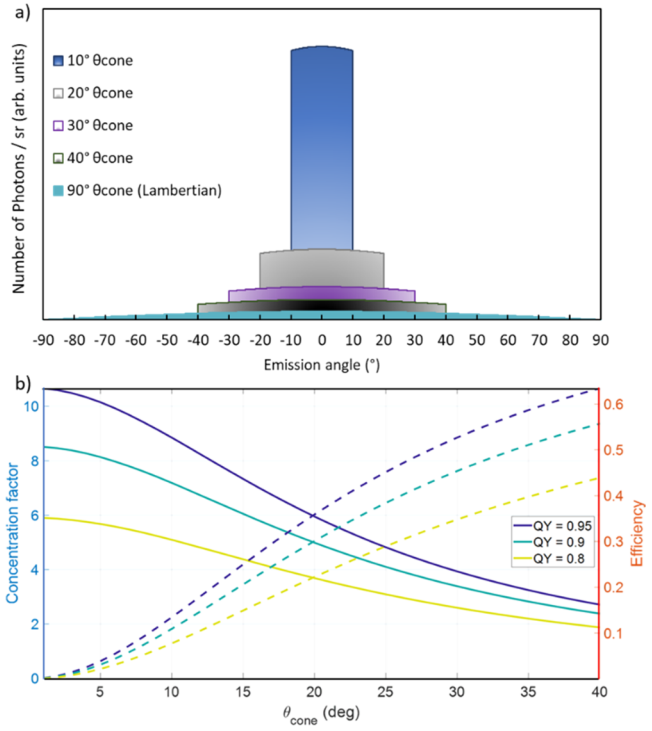

Figure 2. (a) Angle-dependent photon emission distribution for five different emission cones in ideal systems with unity efficiency. (b) Concentration factor (solid lines, left ordinate) and efficiency (dashed lines, right ordinate) depending on the escape cone for systems with three different luminophore quantum yields (QY), ideal nanophotonic coating, and realistic properties of all other system components.

redistributed across different angles. Considering purely this loss-free detailed balance case, for an infinitesimal escape cone the concentration would go to infinity. Thermodynamically, such a singularity is not allowed, the maximum concentration C_{max} is limited by the photon energy loss during the down-shift (Stokes-shift) as derived by Yablonovitch:[18]

$$C_{max} \approx \exp\left(\frac{h(\upsilon_1 - \upsilon_2)}{k_b T}\right)$$

where υ_1 and υ_2 are the frequencies of the incoming photon and Stokes-shifted photon, respectively, h is the Planck's constant, k_b is the Boltzmann constant, and T is the temperature. For the dye used in this study, Lumogen Red, the thermodynamic limit would be at a concentration of approximately 100. We will see below that practical losses pose a stricter limit to the concentration and with the available materials, the thermodynamic limit cannot be reached.

The real concentration factor C_{real}, including realistic losses, can be described as the ideal concentration factor multiplied by the system efficiency η_{sys}:

$$C_{real} = \eta_{sys} C_{id}$$

An analytical model describing the system efficiency can be found in the Methods section. The system efficiency is defined as the number of emitted photons divided by the number of incident photons. The higher the concentration, the longer the light will be trapped inside the waveguide and the more loss mechanisms it will encounter. Therefore, the efficiency decreases with decreasing escape cone size. Similarly, in standard luminescent solar concentrators the efficiency decreases with increasing concentration. The concentration that can be achieved with realistic losses and the respective

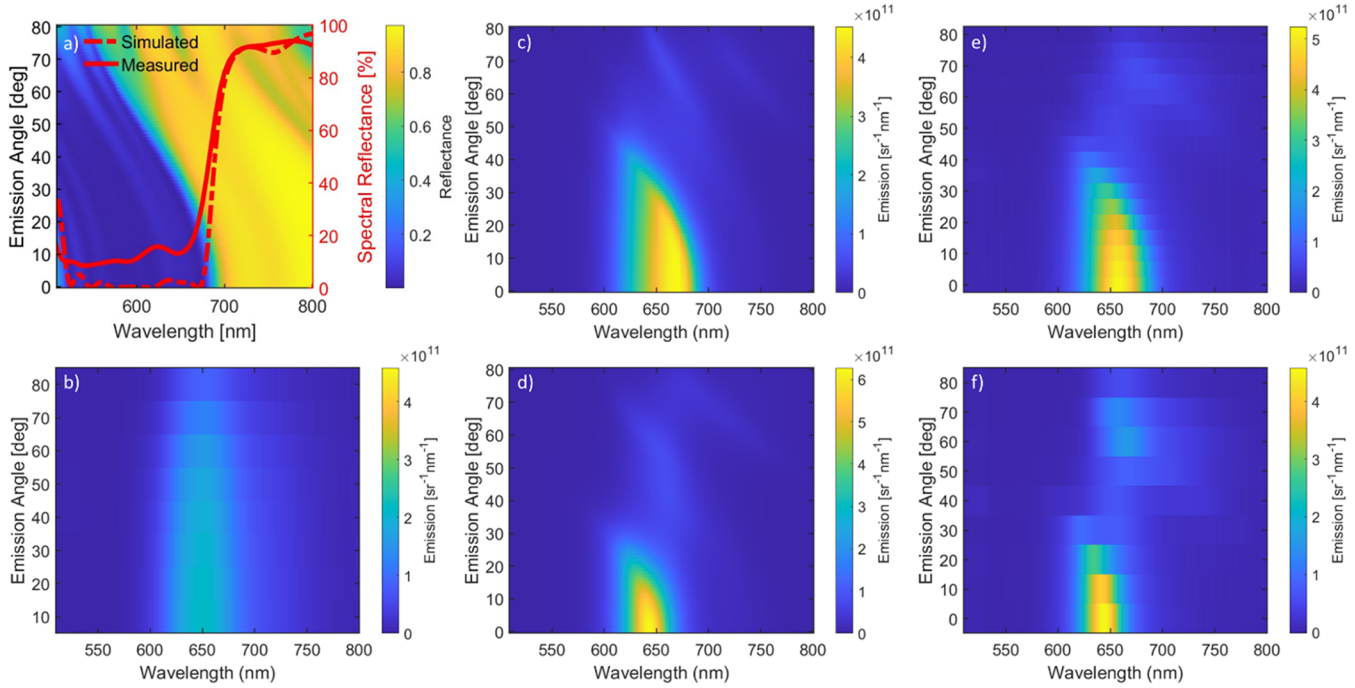

Figure 3. (a) Computationally simulated wavelength and angle dependent reflectance of the nanophotonic coating. The two lines compare the simulated and measured wavelength dependent reflectance at 5° angle of incidence. (b) Measured wavelength and angle-dependent emission of a system that entails a luminophore doped polymer waveguide and a Lambertian back reflector, but no nanophotonic surface coating. Simulated (c, d) and measured (e, f) wavelength and angle-dependent emission of a luminescent free-space concentrator with (c, e) 40° and (d, f) 20° emission cone.

https://doi.org/10.1021/acsphotonics.2c01652
ACS Photonics 2023, 10, 508−517

system efficiency depending on the escape cone half angle are shown in Figure 2b for three different luminophore quantum yields (QY). The other parameters are described in the Methods section and were chosen to be realistically achievable with our materials. Note that contrary to the results presented below, in Figure 2b, the nanophotonic metamaterial was assumed to be ideal, i.e., it ensures that all photons within but no photons outside of the escape cone will escape. High quantum efficiency of all involved processes is crucial to engineer a system that shows concentration, i.e., that has a concentration factor >1 and therefore, will emit more photons within the emission cone than a Lambertian reflector. To obtain good signal-to-noise ratio measurements, we designed our experimental systems for escape cones that should provide us with more than 40% system efficiency. We used a luminophore with a QY of up to 99% and two different escape cones, 20° and 40°, as described in the following section.

Experimental Demonstration and Comparison with Analytical Model. To obtain the desired property of allowing all high energy photons to enter the waveguide while restricting the escape of red-shifted photons outside of the escape cone, a nanophotonic metasurface needs to be designed. Dielectric multilayer stacks are commonly used as notch filters[19] and we chose to work with aperiodic structures to gain full control over the spectral and angular properties. A small refractive index contrast offers high flexibility but requires a large amount of layers, whereas a large refractive index contrast means less layers are necessary, but the spectro-angular properties are less flexible. We chose a material combination that was readily available in our clean room, namely alternating layers of SiO_2 and SiN_xO_y. As explained in the Methods section, we first computationally (inverse) designed the surface before fabricating the real stack in our cleanroom. In Figure 3a the calculated angle and wavelength-dependent reflectance for an optimized surface with an emission cone of 40° at 650 nm are shown. In the Methods section, we provide simulated spectro-angular reflectance for the 20° emission cone and for the case that alternating layers of SiO_2 and TiO_2 would have been used. Absorption of our materials is negligible; hence the angle and wavelength dependent transmittance equals 1 minus the reflectance. Note that due to dispersion, the escape cone within the system (polymer matrix) is smaller than outside of the system. Following reciprocity, a photon incident on this nanophotonic coating from within the system will encounter the same spectrum and angle dependence upon emission into free space, however, the angle dependence will be "squeezed" from the inside due to dispersion and the reflectance is unity for all angles beyond the critical angle for total internal reflection. This was explicitly considered in our model as further explained below.

Figure 3a also shows the simulated and measured wavelength-dependent reflectance at an angle of incidence of 5°. The step locations from low reflectance to high reflectance are nearly identical and the reflectance for long wavelengths match very well. In the short wavelength regime, our simulations predicted slightly lower reflectance possibly due to assuming temporal coherence of light throughout the whole substrate. The emission maximum of Lumogen Red occurs at around 650 nm (see Figures 3b and 4) for which Figure 3a shows an emission cone of approximately 40°. We designed another

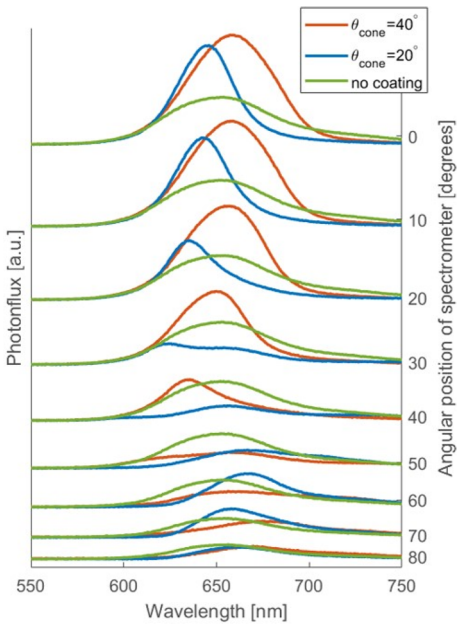

Figure 4. Measured wavelength-dependent photon flux for three different cases: a system with only the Lumogen F Red doped waveguide with Lambertian back reflector and systems with 40° and 20° emission cone nanophotonic coatings added, respectively.

coating with an emission cone of approximately 20° at 650 nm (see Figure 7b in the Methods section).

To prove free-space concentration, we had to carefully design an experiment, which clearly shows the collimation without any artifacts resulting, e.g., from specular reflection. For this, we designed a goniometer as explained in the Methods section and measured wavelength- and angle-dependent system emission with a spectrometer. To quantify the concentration, we took measurements with a close to ideal Lambertian reflector. If for certain angles a photon flux higher than that of the Lambertian reflector can be measured, then our system acts as a collimator. To avoid convoluting specular reflection with our system's emission, we chose an angle of incidence for our light source of 40° which means that specular reflected light was outside or just on the edge of the emission cone. As the light source, we used a green laser with 516 nm wavelength.

In Figure 3b the measured wavelength- and angle-dependent emission of the Lumogen F Red 305 doped PMMA waveguide with a Lambertian back reflector but no nanophotonic coating is shown. The dye emission peaks around 650 nm, and the emission drops with increasing angle as expected from the isotropic nature of the emission.

In Figure 3c,d, the resulting calculated emission for the above-described system are shown dependent on the angle and wavelength for the 40° and 20° emission cone, respectively. It can be seen that the emission peaks around the wavelength at which the Lumogen F Red 305 is emitting strongest and is constrained to an escape cone of around 40° and 20° respectively. Figure 3e and 3f show the experimental results corresponding to the cases shown in 3c and 3d, respectively. The overall distributions of the simulated and measured emission show excellent agreement. In Figure 3c and 3e even the absolute values are very similar. The theory predicted slightly lower emission which could be due to a slight overestimate of the loss mechanisms. For Figure 3f, we see

https://doi.org/10.1021/acsphotonics.2c01652
ACS Photonics 2023, 10, 508−517

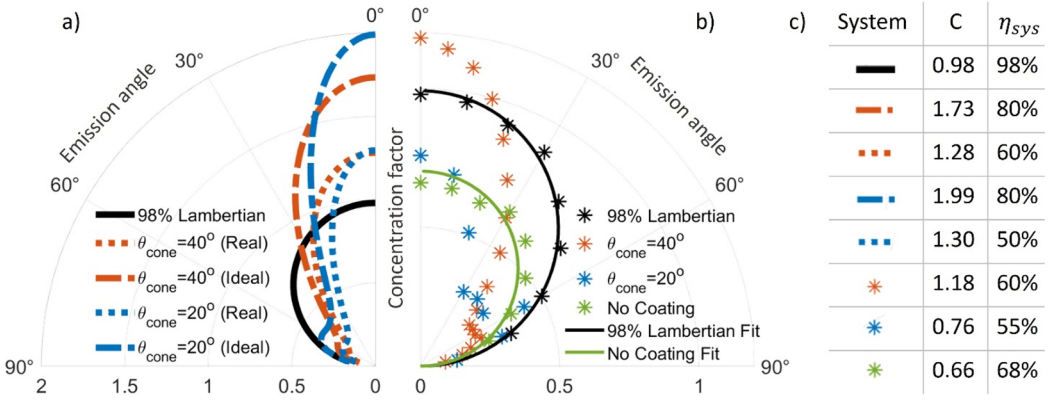

Figure 5. (a) Simulated (lines) and (b) measured (asterisk) and fitted (lines) angle-dependent emission of a 98% reflective Lambertian reflector (black), a dye-doped PMMA waveguide with Lambertian back reflector (green), the full free-space collimation system with 40° (red) and 20° (blue) emission cone, respectively. The experimental 40° emission system clearly shows a higher concentration factor than the Lambertian reflector, thereby experimentally demonstrating free-space diffuse light collimation. Note that the axes in (a) and (b) are different. (c) Table summarizing concentration factor (C) and system efficiency (η_{sys}).

more escape outside of the emission cone and less emission within the emission cone than predicted by simulations (Figure 3d). We will discuss these findings further below.

To facilitate comparison between the three cases: no nanophotonic coating, 40°, and 20° emission cone, we plotted the different cases together in one graph (Figure 4) dependent on the wavelength and for emission angles ranging between 0° and 80°. In particular at angles close to normal incidence, so within the emission cone, it can be seen that the nanophotonic coatings enhance the emission of down-shifted photons. On one hand, this results from internal reflection being suppressed within the emission cone by the nanophotonic coating. On the other hand, the photons with angles outside of the emission cone are reflected back into the system, recycled, randomized and then also emitted within the emission cone. The 40° emission cone nanophotonic surface was nicely designed so the luminophore emission wavelength and the emission cone wavelength have good overlap. Therefore, quite significant emission is achieved at 0°. However, the 20° nanophotonic surface was merely obtained by squeezing the layer stack resulting in the whole pattern to move to shorter wavelengths due to Maxwell's equations' scale invariance. In all honesty, the squeezing of the layer stack was caused by an incorrect tooling factor during the first round of layer depositions. Instead of discarding the sample, we use the measurements here as a very interesting show case of the system properties and of the requirements for high performance. As can be seen from Figure 7b, the 20° emission cone coating does not allow for photons with wavelength greater than 660 nm to leave the system. However, a significant portion of the luminophore emission lies beyond 650 nm. All of these photons are reflected back into the system and recycled with the Lambertian reflector. Unfortunately, this also means that these photons will encounter more loss events, such as incomplete recycling by the 98% efficient Lambertian reflector, luminophore reabsorption, or polymer matrix absorption. On one hand this result confirms our theoretical findings that loss mechanisms become more detrimental the more we restrict the emission cone, on the other hand, this result also stresses the importance of properly matching luminophore emission and emission cone wavelength window to obtain good system performance.

It is instructive to integrate over the wavelength and over the azimuth angle to obtain information on purely the (zenith) angle-dependent photon emission. The result is presented in Figure 5. In Figure 5a, several calculated cases are shown, whereas Figure 5b presents the experimental results and fits. A Lambertian reflector is expected to show cosine behavior and should therefore result in a semicircle when plotted in polar coordinates as can be seen from the black solid line in Figure 5a. Our measurements (black asterisk in Figure 5b) confirm the Lambertian nature of the reflector we used and can be fitted with a cosine model (black solid line in Figure 5b). The luminophore-doped waveguide also shows an isotropic emission as seen by the measured data (green asterisk) and fitted curve (green line) in Figure 5b. The calculated emission profile for the 40° and 20° emission angle coatings are shown in Figure 5a as red and blue dashed lines, respectively. We considered two distinct cases: an ideal scenario in which all processes have unity efficiency and one scenario in which the parameters were chosen to mimic our case, i.e., 99% luminophore quantum yield, 98% Lambertian back reflector, and other losses/parameters as described in the Methods section. The resulting concentration factors (C) and system efficiencies (η_{sys}) as defined above are summarized in Figure 5c. If no losses were present, we would expect our 40° and 20° emission systems to reach a concentration factor of 1.73 and 1.99, respectively. Including losses, we calculated a concentration factor of 1.28 and 1.30 for the 40° and 20° emission systems, respectively. While the loss-free 20° emission system yields a significantly higher concentration, including losses, this benefit almost completely disappears as was to be expected from the results presented in Figure 2b. Figure 5b shows the respective measured data. The 40° emission system surpasses the emission of the Lambertian reflector and yields a concentration factor of 1.18 at 0° emission, thereby experimentally demonstrating the collimation of light in free space. The 20° emission system also shows suppressed emission outside of the emission cone but does not surpass the Lambertian reflector at 0°, the concentration factor is 0.76 and thereby, this system failed to collimate more light within the emission cone than what was sent in. Though, it does have a higher concentration factor than the luminophore doped waveguide (C = 0.66).

To shed more light on the reasons behind the difference in performance between simulated and experimental systems, we calculated the system efficiencies for all structures. As defined

https://doi.org/10.1021/acsphotonics.2c01652
ACS Photonics 2023, 10, 508−517

above, the system efficiency describes the ratio of outgoing to incoming photons. The number of outgoing photons was obtained by integrating the emission over all wavelengths and over the whole upper hemisphere assuming spherical symmetry. The incoming photon number was calculated by integrating over all wavelengths and angles of the photons reflected by the Lambertian reflector and assuming an efficiency of 98% for the Lambertian. This integration and normalization resulted in 7.1×10^{13} photons/s/cm^2 of incoming photons. The efficiencies of all systems are summarized in Figure 5c. The 40° emission system had a system efficiency of 60% as predicted by the theory. Nevertheless, the experimental concentration factor is slightly lower which can be explained by some escape outside of the emission cone at shallow angles which was not expected from simulations. The 20° emission system had a system efficiency of 55% which was higher than expected from simulations (50%). Nevertheless, the concentration factor was lower than expected from simulations. As already observed in Figure 3f, the 20° system had non-negligible escape outside of the escape cone, which lowered the concentration factor but on the other hand increased the efficiency due to less restriction and therefore less encounters with loss mechanisms. For the same reasons, the luminophore-doped waveguide without nanophotonic coating had the highest system efficiency (68%) of all measured systems but the lowest concentration factor (0.66).

Conclusions. In this paper, we have shown the concept, analytical model and experimental demonstration of free-space diffused light concentrators. The maximum possible photon concentration within a desired solid angle depends on the size of the emission cone. Ideally, the smaller this cone, the higher the concentration that can be achieved. However, real systems exhibit losses which increase in severity the higher the concentration. These losses reduce the overall system efficiency and put a practical limit to the concentration. We experimentally presented two free-space collimation systems, one with 40° and one with 20° emission cone. The 40° emission cone system yielded a concentration factor of 1.18, thereby experimentally demonstrating collimation of diffused light in free space. Our analytical model and our experimental results are in excellent agreement enabled by accurate analysis of the optical materials properties and by a rigorous model accounting for a vast majority of loss mechanisms. Slight deviations can be explained by the nanophotonic coatings allowing emission outside of the escape cone which was not accounted by the simulations. We see great potential to further reduce losses through controlling the angular emission of the luminophores, similar to studies on conventional luminescent concentrators,[20,21] by engineering the local optical density of states. Free-space diffuse light concentrators can greatly enhance the yield and application areas of photovoltaic solar energy harvesting systems and might play an important role for a sustainable future.

METHODS

Analytical Model to Calculate the System Efficiency.[17] The system efficiency is defined as the number of emitted photons divided by the number of incident photons. The light has to "flow" through multiple states in the device before it can be emitted in the escape cone. The incident light has to enter the structure, be absorbed by the luminophores, may be reflected at either the top, bottom, or both surfaces, before it escapes. These "steps" describe how the light moves through the system. It is the knowledge of these "states" and "steps" that are at the core of the analytical model describing the system efficiency. The photon flux at the states that the light can be in are labeled as follows: I1, Incoming light; I2, Light absorbed by luminophores; I3, Bottom of waveguide; I4, Top of waveguide; I5, Light inside the desired escape cone.

These states are schematically shown in Figure 6. Arrows indicate the available paths between the states. For example,

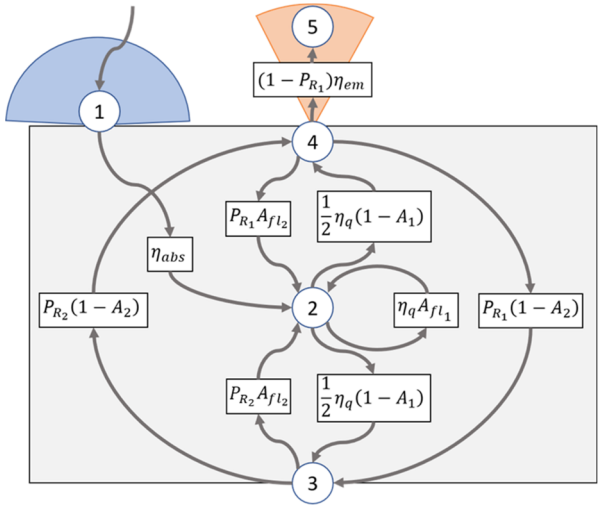

Figure 6. Schematic representation of the paths that photons can take in free-space luminescent solar concentrator. Each circle represents a "state" of the light and each rectangle depicts a "step".

the arrow between I4 and I3 shows the light that moves between the top and bottom surface. The arrow from I4 to I2 shows light that is reflected at the top surface, and that is absorbed by the luminophores before reaching the bottom. The arrow from I1 to I2 shows the absorption of the incoming light. There is a constant flow of light into the system, this is shown by the arrow going into I1. Together, the arrows show all of the possible paths that the light can take. Knowing the direction and possibilities of the energy flow is not enough, the flow has to be quantified in order to calculate the total system efficiency. This is done by assigning magnitudes to the arrows based on the loss mechanisms. For example, the arrow between I4 and I3 is the fraction of light that is incident on the top that is both reflected at the top surface (probability of P_{R_1}) and also not absorbed within the waveguide matrix (probability of $1 - A_2$). These conditions can be combined to get the magnitude of the arrow: $\|4 \rightarrow 3\| = P_{R_1}(1 - A_2)$. Another example is the arrow between I2 and I3, which is the fraction of the absorbed light that is re-emitted (probability of η_q) downward (probability of 1/2) and not absorbed before it reaches the next node (probability of $1 - A_1$). Thus, the amplitude of that arrow is $\|2 \rightarrow 3\| = 1/2\eta_q(1 - A_1)$.

Using this type of reasoning, it is possible to deduce the magnitude of all arrows. η_{em} is the fraction of emitted photons that is emitted in the desired escape cone, η_{abs} is the fraction of photons absorbed by the luminophores, A_{fl1} is the immediate reabsorption by the luminophores, and A_{fl2} is the absorption by the luminophores after the photon was reflected by either top or bottom surface.

Figure 6 shows the photon flow diagram as well as the magnitudes of all arrows. One important aspect of the diagram

https://doi.org/10.1021/acsphotonics.2c01652
ACS Photonics 2023, 10, 508−517

is the fact that the sum of all outgoing arrows is always less than or equal to one. This condition is equivalent to physical conservation of energy. If the arrows sum to one, then the state is lossless, i.e., all light that enters the state reaches another state. As one example, for state 2, this would be the case if the luminophores had a perfect quantum yield of 1. If the arrows sum to some value smaller than one, light is lost from that node. An example is nonideal reflectance at the bottom surface, where light escapes out of the system. Next, this diagram can be converted into a system of linear equations as explained in reference.[17] In Figure 2b, both the concentration factor as well as the system quantum efficiency are shown dependent on the escape cone and for luminophore quantum yield of 0.8, 0.9, and 0.95, respectively. The quality factor, i.e., the ratio between the molar absorption at 516 nm and the molar reabsorption coefficient was set to 20 and the Lambertian rear reflector was set to reflect 98%. For decreasing escape cone the efficiency decreases and converges to 0. At the same time the concentration factor reaches a maximum which is limited to a finite value due to the efficiency approaching 0. For high concentration, the photons need to remain for a long time in the waveguide and therefore, have high chance of interacting with a loss mechanism before meeting the conditions for escape.

Analytical Model Spectro-Angular Emission. To model the spectrum and angle dependent emission of the full device, we need to know (1) the wavelength-dependent luminophore emission, (2) the spectro-angular transmission of the nanophotonic coating, and (3) the overall system efficiency as calculated in the previous section. Knowing (1) and (2) will give us the right trend and qualitative agreement with the experimental results, but the absolute values depend on the system efficiency. In the model, the incoming photons are converted to a longer wavelength according to the luminophore emission spectrum. We used our measured Lumogen Red emission spectrum shown in Figures 3b and 4 at 0° emission without any nanophotonic coating. We make the assumption that without any nanophotonic coating, the emitted spectrum on the outside of the waveguide corresponds to the spectrum of the lumiphores within the waveguide. Within the narrow wavelength regime of the dye emission, the refractive index of the matrix material is constant, and therefore the escape out of the waveguide should not depend on the photon wavelength. The absolute (wavelength integrated) photon flux of emitted photons is calculated by multiplying the number of incoming photons by the system efficiency. Then, to calculate the spectro-angular emission, the photons emitted by the dye are distributed over the different angles weighted according to the angle dependent transmittance (1-reflectance) of the nanophotonic coating at each wavelength. It should be noted that the distribution of photons outside of the waveguide indeed follows the angle dependent transmittance as discussed above. However, to calculate how many photons will leave the waveguide, the angular dependent transmittance from within the waveguide needs to be taken into account. Due to the refractive index of the matrix material being higher than that of air, there will be a critical angle for total internal reflection and all the other angles will become smaller according to Snell's law. The reflectance from within the PMMA matrix for the 40° emission cone is shown in Figure 7. This also demonstrates that by decreasing the refractive index of the matrix, we could allow more photons to exit within the desired cone and thereby further decrease losses.

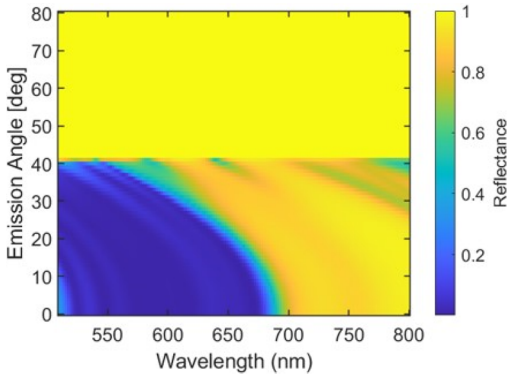

Figure 7. Spectro-angular reflectance of the nanophotonic surface for the 40° emission cone as experienced by photons exiting the waveguide.

The above-described analytical models are openly available on github (github.com/ShwetaPal16/FSLSC_AnalyticalSolution).

Nanophotonic Coating Design and Fabrication. We employed the transfer matrix method to computationally determine the reflectance, transmittance and absorbance of this stack[22] using the refractive index data from films fabricated and measured in our cleanroom via plasma enhanced chemical vapor deposition (PECVD) on 4 in. quartz wafers. The wavelength dependent complex refractive indices were obtained by ellipsometry measurements. We obtained the layer thicknesses from an inverse optimization using the particle swarm method as explained by Poli et al.[23] All simulations were performed for TE and TM polarized light and the results presented in this paper are the average of both polarizations. The resulting nanophotonic coating consists of a dielectric thin film multilayer-stack made of 26 layers of alternating SiO_xN_Y and SiO_2 with complex thickness distribution (see Figure 8a). We chose for these materials as they were readily available in our cleanroom for deposition with high quality material parameters, i.e., with virtually no parasitic absorption. We measured the refractive index of SiO_xN_Y to be 1.92 and the one of SiO_2 to be 1.48, both at 600 nm incident light. This rather low refractive index contrast required to use 26 layers. Figure 8b shows the wavelength and angle dependent reflection for a coating designed for a 20° emission cone at 650 nm. As mentioned before, we primarily worked with the materials that were available in our clean room. However, we also performed simulations for another common set of materials with larger refractive index contrast, namely SiO_2 and TiO_2. In Figure 9, we show the spectro-angular reflectance for a 10 layer (Figure 9a), 14 layer (Figure 9b), and 18 layer (Figure 9c) system. Already in the 10 layer system, the overall trend is visible, but the contrast is not as good as in the systems with more layers. In particular, the one with 18 layers has a steep transition from very transparent to highly reflective at around 700 nm. This very sharp contrast and steep transition is important to avoid losses. Comparing the 18 layers SiO_2/TiO_2 with the 26 layers SiO_2/SiO_xN_Y shows that with higher index contrast materials, we can achieve a high reflectance contrast with less layers, however, the transparency in the short wavelength regime is not as good, there are ripples with non-negligible reflectance. In a future study, we intend to find the optimum multilayer stack taking the luminophore emission and absorption as well as the incoming solar spectrum into account.

https://doi.org/10.1021/acsphotonics.2c01652
ACS Photonics 2023, 10, 508−517

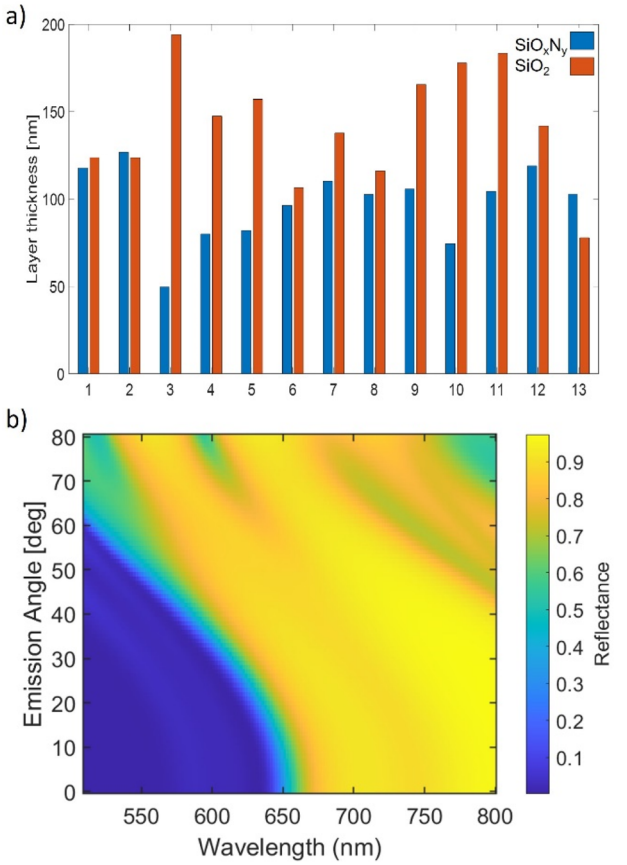

Figure 8. (a) Layer thicknesses of the nanophotonic surface coating. (b) Spectro-angular reflectance of the 20° emission cone coating.

Fabrication of Luminescent Waveguides. Poly(methyl methacrylate) (PMMA) waveguides doped with Lumogen F Red 305 dye were fabricated dissolving PMMA granulates and the dye in toluene, subsequently mixing the two solutions and curing the mixture at room temperature in a mold. To avoid bubbles and ensure proper curing, the desired thickness was reached by casting thin layers which were let to cure before the next layer was cast. We tested different concentrations of PMMA and dye to obtain the optimal dye concentration. The measurements shown in this paper were performed with a concentration of 38.1 ppm of Lumogen F Red 305 dye in PMMA.

UV−Vis Reflection Measurements. Reflection measurements were performed with a PerkinElmer Lambda 950 UV−vis spectrometer. Samples were put on the exit port of an integrating sphere and the measurement beam was incident under 5°. The measurements were calibrated using a Spectralon sample with known reflectivity as 100% reference.

Spectro-Angular Emission Measurements. To measure the wavelength and angle dependent emission, we built an optical goniometer in which we can independently set the incident angle of the exciting light source and the angle under which a calibrated fiber coupled spectrometer (Avantes CMOS device, with a bandwidth of 200 to 1100 nm, and accuracy of ±5%) measures the emitted intensity and spectrum. Here, we used a green laser (516 nm) for excitation. To prove the collimating property of the device without convoluting specular reflection, we shone the laser from a 40° angle, which means that the specular reflection peak fell outside or just on the edge of the emission cone and did not contribute to the calculation of the concentration factor. Furthermore, reflected and emitted light could also be deconvoluted through their different wavelengths, the reflected light peaking at 516 nm (laser emission) and the emitted light peaking around 650 nm (dye emission). Note that all results are reported in photon flux as we would like to determine the systems quantum efficiency. Due to the energy down-shifting, the energy efficiency is lower than the quantum efficiency. In other words, if every green photon was converted into one red photon, our quantum efficiency would be 100%. The energy efficiency would be lower as the photons lose part of their energy in the process which is thermodynamically necessary to allow for collimation and concentration as explained above.

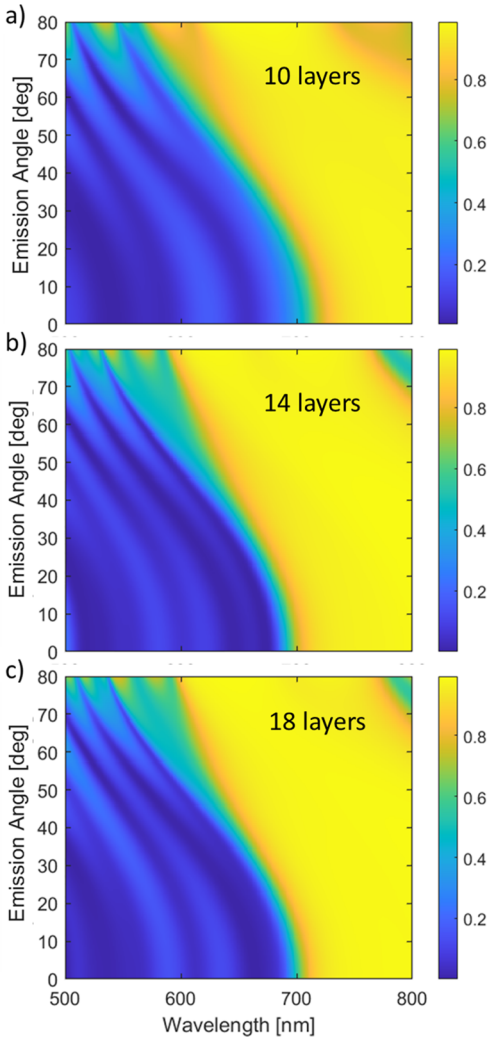

Figure 9. Simulated spectro-angular emission for optimized SiO_2/TiO_2 multilayer stacks with (a) 10, (b) 14, and (c) 18 layers.

To enable modular experiments in which parameters can easily be changed while keeping others constant, we designed the system such that the Lambertian back reflector, the Lumogen F Red 305 doped PMMA waveguide and the nanophotonic coating were separate samples mechanically pressed together with a clamp. To avoid total internal reflection within the waveguide, we roughened the back surface of the waveguide and we put an index matching fluid (water) in between the waveguide and the nanophotonic coating.

https://doi.org/10.1021/acsphotonics.2c01652
ACS Photonics 2023, 10, 508−517

■ ASSOCIATED CONTENT

Data Availability Statement

The data that underlie the plots within this paper and other findings of this study are available on data.4tu.nl, github, and from the corresponding author on reasonable request.

■ AUTHOR INFORMATION

Corresponding Author

Rebecca Saive − *MESA+ Institute for Nanotechnology, Inorganic Materials Science, University of Twente, 7522 NB Enschede, Netherlands*; orcid.org/0000-0001-7420-9155; Email: r.saive@utwente.nl

Authors

Lisanne M. Einhaus − *MESA+ Institute for Nanotechnology, Inorganic Materials Science, University of Twente, 7522 NB Enschede, Netherlands*

Geert C. Heres − *MESA+ Institute for Nanotechnology, Inorganic Materials Science, University of Twente, 7522 NB Enschede, Netherlands*

Jelle Westerhof − *MESA+ Institute for Nanotechnology, Inorganic Materials Science, University of Twente, 7522 NB Enschede, Netherlands*

Shweta Pal − *MESA+ Institute for Nanotechnology, Inorganic Materials Science, University of Twente, 7522 NB Enschede, Netherlands*

Akshay Kumar − *MESA+ Institute for Nanotechnology, Inorganic Materials Science, University of Twente, 7522 NB Enschede, Netherlands*

Jian-Yao Zheng − *MESA+ Institute for Nanotechnology, Inorganic Materials Science, University of Twente, 7522 NB Enschede, Netherlands*

Complete contact information is available at: https://pubs.acs.org/10.1021/acsphotonics.2c01652

Author Contributions

R.S. proposed the project and conceptually designed the free-space luminescent concentrator and measurements thereof. L.E. designed the nanophotonic coating and made a first analytical description of the system. G.H. improved the analytical description. A.K. fabricated Lumogen Red dye doped PMMA waveguides. J.W., J.Z., and S.P. performed spectro-angular emission measurements and UV−vis reflection measurements. J.W. also performed most of the measurement data analysis. S.P. also advised with simulations and data analysis.

Author Contributions

†These authors contributed equally to this work.

Funding

The authors acknowledge funding through TTT-plan Thematische Kennisoverdrachtsplan Circulaire Economy, subsidiebeschikking TTT19002.

Notes

The authors declare no competing financial interest.

■ ACKNOWLEDGMENTS

The authors would like to thank Bryce Richards (KIT) and Peter Erk (BASF) for providing materials and helpful discussions. Furthermore, we thank Peter Linders for PECVD deposition and Dominic Post for help with setting up experiments. R.S. would like to thank David Needell (Columbia University) and Harry Atwater (Caltech), Eli Yablonovitch (UC Berkeley), Albert Polman, and Erik Garnett (both AMOLF), and Muhammad Ashraful Alam (Purdue University) for fruitful discussions. We thank Sebastian Husein for proof-reading the manuscript.

■ REFERENCES

(1) Smestad, G.; Ries, H.; Winston, R.; Yablonovitch, E. The thermodynamic limits of light concentrators. *Solar Energy Materials* **1990**, *21*, 99−111.

(2) Markvart, T. The thermodynamics of optical étendue. *Journal of Optics A: pure and applied optics* **2008**, *10*, 015008.

(3) Shockley, W.; Queisser, H. J. Detailed balance limit of efficiency of p−n junction solar cells. *Journal of applied physics* **1961**, *32*, 510−519.

(4) Durmaz, Z. H. Thin silicon interference solar cells for targeted or broadband wavelength absorption enhancement. *Opt. Express* **2021**, *29*, 4324−4337.

(5) Saive, R. Light trapping in thin silicon solar cells: a review on fundamentals and technologies. *Progress in Photovoltaics: Research and Applications* **2021**, *29* (10), 1125−1137.

(6) Rapp, C. F.; Boling, N. L.*13th Photovoltaic Specialists Conference*, Washington, DC, June 5−8, 1978, IEEE, 1978; pp 690−693.

(7) Weber, W. H.; Lambe, J. Luminescent greenhouse collector for solar radiation. *Applied optics* **1976**, *15*, 2299−2300.

(8) Goetzberger, A.; Greube, W. Solar energy conversion with fluorescent collectors. *Applied physics* **1977**, *14*, 123−139.

(9) Green, M.; Dunlop, E.; Hohl-Ebinger, J.; Yoshita, M.; Kopidakis, N.; Hao, X. Solar cell efficiency tables (version 57). *Progress in photovoltaics: research and applications* **2021**, *29*, 3−15.

(10) Green, M. A.et al.Solar cell efficiency tables (Version 60). *Progress in Photovoltaics: Research and Applications30*, 687−701, DOI: 10.1002/pip.3595 (2022).

(11) Slooff, L. H.; Bende, E. E.; Burgers, A. R.; Budel, T.; Pravettoni, M.; Kenny, R. P.; Dunlop, E. D.; Buchtemann, A. A luminescent solar concentrator with 7.1% power conversion efficiency. *Physica Status Solidi (RRL)* **2008**, *2*, 257−259.

(12) Tummeltshammer, C.; Taylor, A.; Kenyon, A. J.; Papakonstantinou, I. Losses in luminescent solar concentrators unveiled. *Sol. Energy Mater. Sol. Cells* **2016**, *144*, 40−47.

(13) Geisz, J. F.; et al. Building a six-junction inverted metamorphic concentrator solar cell. *IEEE Journal of Photovoltaics* **2018**, *8*, 626−632.

(14) Russell, T. C.; Saive, R.; Augusto, A.; Bowden, S. G.; Atwater, H. A. The Influence of Spectral Albedo on Bifacial Solar Cells: A Theoretical and Experimental Study. *IEEE Journal of Photovoltaics* **2017**, *7*, 1611−1618.

(15) Pal, S.; Reinders, A.; Saive, R. Simulation of Bifacial and Monofacial Silicon Solar Cell Short-Circuit Current Density Under Measured Spectro-Angular Solar Irradiance. *IEEE journal of photovoltaics* **2020**, *10*, 1803−1815.

(16) Miller, O. D.; Yablonovitch, E.; Kurtz, S. R. Strong internal and external luminescence as solar cells approach the Shockley−Queisser limit. *IEEE Journal of Photovoltaics* **2012**, *2*, 303−311.

(17) Heres, G. C.; Einhaus, L. M.; Saive, R.*2021 IEEE 48th Photovoltaic Specialists Conference (PVSC)*, June 20−25, 2021, IEEE, 2021; pp 1027−1029.

(18) Yablonovitch, E. Thermodynamics of the fluorescent planar concentrator. *JOSA* **1980**, *70*, 1362−1363.

(19) Macleod, H. A.; Macleod, H. A.*Thin-Film Optical Filters*; CRC Press, 2010.

(20) Bauser, H. C.; et al. Photonic crystal waveguides for> 90% light trapping efficiency in luminescent solar concentrators. *ACS Photonics* **2020**, *7*, 2122−2131.

(21) van der Burgt, J. S.; et al. Unlocking Higher Power Efficiencies in Luminescent Solar Concentrators through Anisotropic Luminophore Emission. *ACS Appl. Mater. Interfaces* **2021**, *13*, 40742−40753.

(22) Einhaus, L.; Saive, R.*2020 47th IEEE Photovoltaic Specialists Conference (PVSC)*, June 15−Aug 21, 2020, IEEE, 2020; pp 1368−1370.
(23) Poli, R.; Kennedy, J.; Blackwell, T. Particle swarm optimization. *Swarm intelligence* **2007**, *1*, 33−57.

https://doi.org/10.1021/acsphotonics.2c01652
ACS Photonics 2023, 10, 508−517